European **J**ournal of **Chem**istry

Check for updates

Crystal structures, computational studies, and Hirshfeld surface analysis on 7-hydroxy-4-methyl-2*H*-chromen-2-one and 7-hydroxy-4-methyl-8-nitro-2*H*-chromen-2-one

Felix Odame [iD] 1,*, Nathaniel Owusu Boadi [iD] 2, Salifu Nanga [iD] 1, Albert Aniagyei [iD] 1 and Eric Hosten [iD] 3

1 *Department of Basic Sciences, School of Basics and Biomedical Sciences University of Health and Allied Sciences, PMB 31, Ho, Ghana*
2 *Department of Chemistry, Kwame Nkrumah University of Science and Technology, Kumasi, Ghana*
3 *Department of Chemistry, Nelson Mandela University, PO Box 77000, Gqeberha 6031, South Africa*

* *Corresponding author at: Department of Basic Sciences, School of Basics and Biomedical Sciences University of Health and Allied Sciences, PMB 31, Ho, Ghana.*
 e-mail: *felixessah15@gmail.com (F. Odame).*

RESEARCH ARTICLE

ABSTRACT

7-Hydroxy-4-methyl-2*H*-chromen-2-one and 7-hydroxy-4-methyl-8-nitro-2*H*-chromen-2-one have been synthesized. The compounds have been characterized using IR, NMR, GC-MS, and elemental analysis. The single-crystal X-ray structure of the compounds showed that compound 1 was crystallized in the orthorhombic space group $P2_12_12_1$ while compound 2 crystalized in the monoclinic space group $P2_1/c$. A comparison of the computed and experimental bond lengths and bond angles showed good agreement among the data. A Hirshfeld surface analysis showed that the H···O/O···H interaction was the most prominent molecular interaction for both compound 1 H···O/O···H (34.4%) and compound **2** H···O/O···H (48.6%).

Cite this: *Eur. J. Chem.* **2025**, *16(3)*, 275-286   Journal website: www.eurjchem.com

1. Introduction

Coumarins have been accessed by several methods, including the Perkin reaction, which involves the reaction of α,β-unsaturated aromatic acid in the presence of sodium acetate followed by intramolecular cyclization to give the expected coumarin [1], Knoevenagel condensation, which involves the reaction between salicylaldehydes and 1,3-dicarbonyl compounds in the presence of a base or an energy source [2], Pechmann condensation, which involves the condensation of β-ketonic esters with phenols in the presence of concentrated sulfuric acid [3]. Wittig reaction, which involves an intramolecular cyclisation of a substituted 2-formylphenyl 2-bromoacetate in saturated aqueous sodium bicarbonate [4], Baylis-Hillman reaction, which involves the reaction of 2-hydroxybenzaldehydes with the methyl acrylate in the presence of DABCO (1,4-diazabicyclo[2.2. 2]octane) [5]. Claisen rearrangement, which involves rearrangement of the 3,3-dimethylallyl ether in the presence of butyric anhydride, has been used to synthesize some coumarin compounds [6], and

Vilsmeier-Haack and Suzuki cross-coupling reactions [1-8]. Coumarins have been reported to exhibit a wide spectrum of inhibitory properties [9-14]. They are known to have antibacterial [15-21] and antifungal activities [19,21-25]. Coumarins have also been reported to be anti-inflammatory [26,27], anti-HIV [10,28], anticancer [11,29,30], antituberculosis [31], anticoagulant [32], antiviral [33] and antihyperglycemic [34]. Several coumarin compounds have been reported to have appreciable antioxidant activity [35-38].

Coumarin derivatives are known as acetylcholinesterase inhibitors (AchE) inhibitors that can also be used to treat Alzheimer's disease [39-41]. The nitro group has been reported to undergo tautomerism in certain scaffolds such as thiones [42]. Different methods have been used to study tautomerism, spectroscopy has been used to study tautomerism in some thiosemicarbazones, and it has been confirmed with DFT calculations [43]. Solvents and substituents have been reported to play an important role in tautomerism.
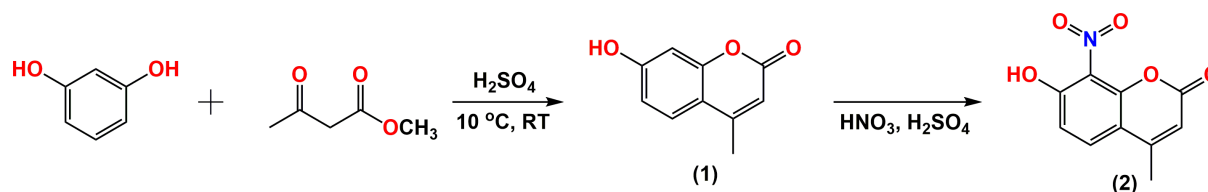
Scheme 1. Synthesis of 7-hydroxy-4-methyl-2*H*-chromen-2-one (1) and 7-hydroxy-4-methyl-8-nitro-2*H*-chromen-2-one (2).

In a study of substituents and solvent effects on the spectral properties of some substituted 4-hydroxycoumarin-derived compounds, the highest quantum fluorescence yield was observed to be apparent for scaffolds containing dimethyl-amino and acetamido groups as attachments to the phenyl ring [44].

This study reports the synthesis, crystal structures, and Hirshfeld surface analysis of 7-hydroxy-4-methyl-2*H*-chromen-2-one and 7-hydroxy-4-methyl-8-nitro-2*H*-chromen-2-one. A discussion of the XRD data of the compounds has been presented to provide insight into the structural properties of the compounds. Hirshfeld surface analysis has been performed on the compounds. The study is part of a continuing study on the development of xazepine-linked coumarins compounds as potential anticancer and antimicrobial agents. This work effectively confirms the basic scaffold on which the xazepine moiety can be mounted for testing.

2. Experimental

2.1. Reagents and instrumentation

Analytical grade reagents and solvents for synthesis such as salicylaldehyde and ethyl acetoacetate were obtained from Sigma-Aldrich (USA), while ethanol and DMSO were obtained from Merck Chemicals (SA). The chemicals were used as received without further purification. ^1H NMR and ^{13}C NMR spectra were recorded on a Bruker Avance AV 400 MHz spectrometer operating at 400 MHz for ^1H and 100 MHz for ^{13}C using DMSO-d_6 as solvent and tetramethylsilane as internal standard. Chemical shifts are expressed in ppm. FT-IR spectra were recorded on a Bruker Platinum ATR Spectrophotometer Tensor 27. Elemental analyzes were performed using a Vario Elementar Microcube ELIII. Melting points were obtained using a Stuart Lasec SMP30 while the masses were determined using an Agilent 7890A GC System connected to a 5975C VL-MSC with electron impact as the ionization mode and detection by a triple-axis detector. The GC was fitted with a 30 m × 0.25 mm × 0.25 μm DB-5 capillary column. Helium was used as carrier gas at a flow rate of 1.63 mL/min with an average velocity of 30.16 cm/s and a pressure of 63.73 kPa.

2.2. Synthesis

2.2.1. 7-Hydroxy-4-methyl-2H-chromen-2-one (1)

Resorcinol (37 g, 0.34 mol) and ethyl acetoacetate (45 mL) were dissolved in 200 mL of ethanol in a round bottom flask and placed in an ice bath. Concentrated sulfuric acid (150 mL) was added dropwise with stirring. Stirring was continued for 6 hours during which the reaction was monitored by thin-layer chromatography until the disappearance of the starting materials. The reaction mixture was then transferred to an ice bath and allowed to stand for four hours. The reaction mixture was filtered, dried, and the product recrystallized as a white solid in ethanol. Colour: White. Yield: 82%. M.p. = 189-190 °C. IR (v_{max}, cm^{-1}): 3123 (OH), 1676 (C=O), 1598 (C=C), 1560 (C=C), 1449 (C-C), 1388 (C-O). ^1H NMR (400 MHz, DMSO-d_6, δ, ppm): 10.51 (br, 1H, OH), 7.59 (d, 1H, *J* = 8.8 Hz, Ar-H), 6.80 (d, 1H, *J* =

8.8 Hz, 1H, Ar-H), 6.70 (1H, Ar-H), 6.11 (1H, Ar-H), 2.36 (s, 3H, CH$_3$). ^{13}C NMR (100 MHz, DMSO-d_6, δ, ppm): 161.6 (C=O), 160.9 (C=O), 155.4 (C), 154.0 (C), 127.1 (CH), 113.3 (CH), 112.5 (C), 110.7 (CH), 102.5 (CH), 18.7 (CH$_3$). GC-MS (*m/z*, M$^+$): 176.06, % 82.3. Anal. calcd. for C$_{10}$H$_8$O$_3$: C, 68.18; H, 4.58; O, 27.25, Found: C, 68.10; H, 4.51; O, 27.18%.

2.2.2. 7-Hydroxy-4-methyl-8-nitro-2H-chromen-2-one compound with (methylsulfinyl)methane (1:1) (2)

Compound 1 (10 g) was dissolved in 50 mL of ethanol, a mixture of HNO$_3$ (5 mL) and H$_2$SO$_4$ (15 mL) was added dropwise with stirring for four hours, during which the reaction was monitored by thin layer chromatography until the disappearance of the starting material. The reaction mixture was transferred to an ice bath filtered and dried under vacuum. The product was dissolved in ethanol and extracted with acetic acid to obtain the 8-nitro derivative. The product was recrystallized and obtained as a yellow solid from DMSO: toluene (4:1, v:v) (Scheme 1). Color: Yellow. Yield: 79%. M.p.: 252-256 °C. IR (v_{max}, cm^{-1}): 3282 (OH), 3055 (C–H), 1733 (C=O), 1616 (C=C), 1568 (C=C), 1506 (C=C), 1348 (C-N), 1322 (C-N). ^1H NMR (400 MHz, DMSO-d_6, δ, ppm): 12.14 (br, 1H, OH), 8.25 (s, 1H, OH), 7.78 (d, *J* = 8.8 Hz, 1H, Ar-H), 7.56 (d, *J* = 8.8 Hz, 1H, Ar-H), 7.02 (d, *J* = 9.2 Hz, 1H, Ar-H), 6.80 (d, *J* =10.2 Hz, 1H, Ar-H), 6.59 (s, 1H, N-OH), 6.28 (s, 1H, Ar-H) 6.11 (s, 1H, Ar-H), 2.40 (s, 3H, CH$_3$), 2.35 (s, 3H, CH$_3$). ^{13}C NMR (100 MHz, DMSO-d_6, δ, ppm): 161.61 (C=O), 160.74 (C=O), 158.54 (C), 155.28 (CH), 154.00 (CH), 152.85 (CH), 146.09 (C), 128.54 (CH), 127.03, (CH), 113.30 (CH), 112.44 (C), 111.72 (CH), 110.70 (CH), 102.62 (CH), 18.73 (CH$_3$), 18.54 (CH$_3$). GC-MS (*m/z*, M$^+$): 221.09, %78.1. Anal. calcd. for C$_{12}$H$_{13}$NO$_6$S: C, 48.16; H, 4.38; N, 4.68; Found: C, 48.07; H, 4.31; N, 4.60%.

2.3. X-ray crystallographic measurements

Using a Bruker Kappa APEX II diffractometer and monochromated MoKα radiation (λ = 0.71073 Å), an X-ray diffraction investigation of the compounds was carried out at 200 K. Data collection was carried out using APEXII [45], and cell refinement and data reduction were carried out using SAINT software [46]. Using SHELXL [45] as a graphical interface, the structures were solved directly using SHELXS-2013 [45] and then refined using least squares techniques using SHELXL-2013 [46]. Anisotropic refinement was used for all non-hydrogen atoms. Uiso (H) was set to 1.2Ueq (C) and carbon-bound H atoms were included in the refinement in the riding model approximation, with predicted positions (C-H = 0.95 Å for aromatic carbon atoms and C-H = 0.99 Å for methylene groups). With Uiso (H) set to 1.5Ueq (C), the H atoms of the methyl groups were allowed to spin around the C-C bond at a fixed angle to best fit the observed electron density (HFIX 137 in the SHELX program suite [46]). On the Fourier map, nitrogen-bound H atoms were found and could be freely refined. The numerical method used in SADABS was used to adjust the data for absorption effects [47]. ORTEP-3 [48] was used to create molecular visuals, while Mercury [49] and PLATON [50] were used to produce the publication data.
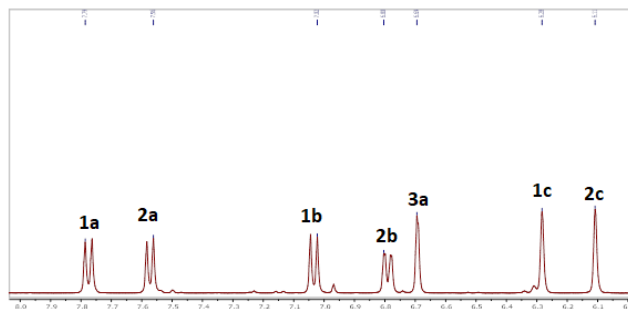
Figure 1. Expanded ^{1}H NMR spectrum of compound 2 indicating the doubling of the proton signals.

2.4. Computational studies

The Gaussian 09 program was used to perform the calculations. Singlet ground state molecular geometries of all compounds were completely optimized in the gas phase in density functional theory (DFT) using the 6-311G(d,p) basis set and the B3LYP, CAM-B3LYP, B3PW91, wB97XD and M06 functionals [51-53]. To ensure that the improved molecular structure matched the minimum energy, optimization and frequency calculation were performed. Gauss view 6.0 or Avogadro were used to view the results. The optimized frequencies were computed using the Gaussian 09 program [54].

The HOMO indicates the ability to donate an electron, while the LUMO indicates the ability to accept an electron. The energy of the HOMO is directly related to the ionization potential, while the energy of the LUMO is related to the electron affinity. The difference in energy between the HOMO and LUMO orbitals, which is the energy gap, decides the stability or reactivity of the molecules [55]. The energy gap is an important parameter in determining molecular electrical transport properties because it is a measure of electron conductivity [56]. The hardness of a molecule also corresponds to the energy gap between the HOMO and LUMO orbitals.

The molecular electrostatic potential (MEP) gives a description of the potential energy that affects a unit positive charge (like a proton) when placed at a certain point in the environment of a molecule. [57-58] It gives maps of the electron density distribution of a molecule, revealing regions of positive and negative potential, which correspond to electrophilic and nucleophilic sites, respectively [59]. Contours of equal value in a selected plane are used to represent MEP values calculated around a molecule.

3. Results and discussion

3.1. Synthesis and reaction mechanism

Compound 1 was obtained by the reaction of resorcinol with ethyl acetoacetate in the presence of an acid catalyst. The product was obtained as white crystals from ethanol. Compound 2 was obtained by reacting compound 1 with mixed acids (HNO_3 and H_2SO_4). The 6-nitro and 8-nitro derivatives were separated by dissolving the dried product in ethanol and extracting with a mixture of toluene: acetic acid (60:40, v:v). The product was recrystallized as a yellow solid from DMSO: toluene mixture (4:1, v:v).

3.2. Spectroscopic characterization

The IR spectrum of compound 1 showed the presence of an absorption peak at 3123 cm^{-1} for the aliphatic C-H stretch. Peaks were observed at 1676, 1598, 1560 and 1449 cm^{-1} for the C=O, C=C, C=C and C-O absorptions, respectively. The ^{1}H NMR spectrum indicated the formation of a coumarin ring with the incorporation of the methyl group of ethyl acetoacetate confirmed by a signal at δ 2.36 ppm for three protons, a broad signal was observed at δ 10.51 ppm for the hydroxyl group, two singlet signals were observed at δ 6.70 and 6.11 ppm for two aromatic protons. In addition, two doublet signals were observed at δ 7.59 and 6.80 ppm for a proton each. The ^{13}C NMR spectrum of compound **1** showed signals at δ 161.6 and 160.9 ppm for carbonyls. Signals observed at δ 155.4 and 154.0 ppm for aromatic carbons without hydrogen atoms were confirmed in the DEPT 135 spectrum. Four signals were observed at δ 127.1, 113.3, 112.5 and 110.7 ppm for aromatic carbons with protons attached. These signals confirmed the formation of the coumarin ring. A signal was also observed at 18.7 ppm for the incorporation of the methyl group on the coumarin ring.

In compound 2, the IR spectrum confirmed a signal at 3282 cm^{-1} for the hydroxyl group, an absorption was observed at 3055 cm^{-1} for the aromatic C-H stretch, a signal at 1733 cm^{-1} was observed for the carbonyl of a lactone. Signals were observed at 1616, 1568 and 1506 cm^{-1} for the C=C stretch. Absorptions were observed at 1348 and 1322 cm^{-1} for the C-N stretch. The ^{1}H NMR spectrum of compound **2** gave a broad signal at δ 12.14 ppm for the hydroxyl group. Four doublets were observed at δ 7.78, 7.56, 7.02 and 6.80 ppm, indicating a doubling of the peaks from the starting material. Three singlet signals were observed at δ 6.59, 6.28 and 6.11 ppm confirming the disappearance of the proton in the starting material, which has been occupied by the nitro group. The doubling of the peaks confirms the existence of two distinct species in the solution. The extra singlet signal is attributable to an OH signal emanating from the nitro group because of tautomerism. Two singlet signals were observed at δ 2.40 and 2.35 ppm confirming the incorporation of the methyl group. Figure 1 shows the expanded ^{1}H NMR spectrum of compound 2 showing the doubling of the signals as a result of tautomerism of the nitro group.

The ^{13}C NMR of compound **2** gave signals at δ 161.6 and 160.7 ppm for carbonyl. Signals for aromatic carbons without hydrogen atoms were observed at δ 158.5, 155.3, 154.0, 152.9 and 146.1 ppm; this was confirmed by their absence in the DEPT135 spectrum. Signals were observed at δ 128.5, 127.0, 113.5, 113.3, 111.7 and 110.7 ppm for aromatic carbons having hydrogen atoms, these signals were confirmed by their presence in the DEPT spectrum. Two signals were observed at δ 18.7 and 18.5 ppm for the methyl groups. Scheme 2 gives the formation of tautomers in the nitrocoumarin derivative indicating the position of protonation of the possible tautomers.

3.3. Crystal structure analysis

Compound 1 was recrystallized as white crystals from ethanol. The compound crystallized in the orthorhombic space group.

Table 1. Crystal data and details of the structure refinement for compounds 1 and 2.

Parameters	Compound 1	Compound 2
Empirical formula	$C_{10}H_8O_3$	$C_{12}H_{13}NO_6S$
Formula weight (g/mol)	176.16	299.29
Temperature (K)	200(2)	296(2)
Crystal system	orthorhombic	monoclinic
Space group	$P2_12_12_1$	$P2_1/c$
a (Å)	5.2105(2)	7.1648(7)
b (Å)	11.7779(4)	20.229(2)
c (Å)	13.1619(5)	9.5583(9)
α (°)	90	90
β (°)	90	94.975(5)
γ (°)	90	90
Volume (Å³)	807.73(5)	1380.1(2)
Z	4	4
ρ_{calc} (g/cm³)	1.449	1.440
μ (mm⁻¹)	0.108	0.259
F(000)	368.0	624.0
Crystal size (mm³)	0.523 × 0.424 × 0.236	0.407 × 0.259 × 0.186
Radiation	MoKα (λ = 0.71073)	MoKα (λ = 0.71073)
2θ range for data collection (°)	4.64 to 56.76	4.026 to 56.642
Index ranges	-6 ≤ h ≤ 6, -14 ≤ k ≤ 15, -17 ≤ l ≤ 17	-9 ≤ h ≤ 9, 0 ≤ k ≤ 26, 0 ≤ l ≤ 12
Reflections collected	15752	3431
Independent reflections	2012 [R_{int} = 0.0158, R_{sigma} = 0.0101]	3431 [R_{int} = 0.0409, R_{sigma} = 0.0326]
Data/restraints/parameters	2012/0/121	3431/36/222
Goodness-of-fit on F²	1.062	1.044
Final R indexes [I≥2σ (I)]	R_1 = 0.0291, wR_2 = 0.0794	R_1 = 0.0590, wR_2 = 0.1522
Final R indexes [all data]	R_1 = 0.0304, wR_2 = 0.0805	R_1 = 0.0976, wR_2 = 0.1783
Largest diff. peak/hole (e.Å⁻³)	0.25/-0.16	0.49/-0.27
CCDC	2419172	2419173
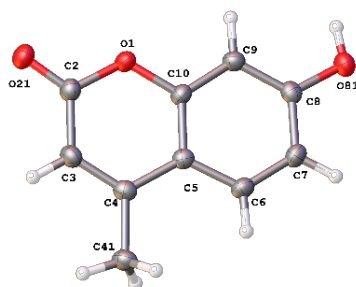
Figure 2. An ORTEP view of 7-hydroxy-4-methyl-2*H*-chromen-2-one (1).
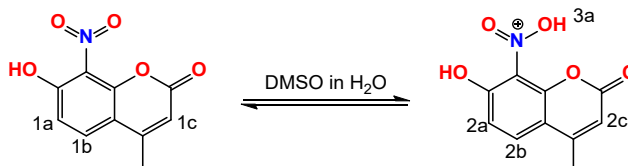
Scheme 2. Formation of tautomers in the nitrocoumarin derivative showing the position of protonation of the possible tautomers.

$P2_12_12_1$ with four molecules in the unit cell characterized by unit cell parameters a = 5.2105(2) (15) Å, b = 11.7779(4) Å, c = 13.1619(5) Å. Compound 2 was recrystallized as yellow crystals from DMSO:toluene (4:1, v:v). The compound crystallized in the monoclinic space group $P2_1/c$ with four molecules in the unit cell characterized by unit cell parameters a = 7.1648(7) Å, b = 20.229(2) Å, c = 9.5583(9) Å, β=94.975(5)°. The ORTEP diagrams for compounds 1 and 2 are presented in Figures 2 and 3. Crystallographic data, and selected bond lengths and bond angles for the compounds are provided in Tables 1 and 2.

3.4. Comparison of theoretical and experimental bond parameters for compound 1

Table 2 gives a summary of theoretical and experimental bond lengths and bond angles for compound 1 using B3LYP, CAM-B3LYP, B3PW91, wB97XD and M06 functionals and the 6-311G (d, p) basis set. The bond lengths of O1-C2, O1-C10, O21-C2 and O81-C8, were experimentally determined as 1.367(2), 1.379(2), 1.220(2) and 1.353(2) Å, respectively, which is consistent with the C=O double bond [60-65], while the calculated bond lengths gave deviations between 0.001 and 0.026 Å from the experimental values. Additionally, the bond angles of C2-C3, C3-C4, C4-C5, C4-C41 and C5-C10 that were experimentally determined as 1.440(2), 1.354(2), 1.446(2), 1.503(2) and 1.402(2) Å, respectively, gave a deviation between 0.001 and 0.010 compared to the calculated bond lengths. The bond lengths of C5-C6, C6-C7, C7-C8, C8-C9 and C9-C10 which were 1.406(2), 1.376(2), 1.401(2), 1.391(2) and 1.386(2) Å, respectively, were consistent with C-C single bonds [60-65], recorded deviations between 0.001 and 0.009 Å when compared with the computed bond lengths. Crystallographically determined bond angles C2-O1-C10, O1-C10-C9, C5-C10-C9, O1-C2-O21, O1-C10-C5 were observed at 121.3(1), 116.1(1), 122.9(1), 116.4(1) and 121.0(1)° while the calculated values gave deviations between 0.1 and 1.4°.

Table 2. Summary of theoretical and experimental bond lengths (Å), and bond angles (°) for 7-hydroxy-4-methyl-2*H*-chromen-2-one (**1**) using B3LYP, CAM-B3LYP, B3PW91, wB97XD and M06 functionals and 6-311G(d,p) basis set (RMS: Root mean square, MAE: Mean absolute error).

| Bond lengths (Å)	Experimental	B3LYP	CAM-B3LYP	B3PW91	wB97XD	M06	Min dev.	Max dev.	RMS	MAE
O1-C2	1.367(2)	1.400	1.385	1.394	1.384	1.391	0.016	0.033	0.0245	0.0238
O1-C10	1.379(2)	1.361	1.357	1.356	1.356	1.353	0.018	0.026	0.0225	0.0224
O21-C2	1.220(2)	1.208	1.203	1.207	1.203	1.203	0.012	0.017	0.0154	0.0152
O81-C8	1.353(2)	1.360	1.354	1.354	1.352	1.350	0.001	0.005	0.0035	0.0026
C2-C3	1.440(2)	1.453	1.454	1.450	1.456	1.448	0.008	0.016	0.0125	0.0122
C3-C4	1.354(2)	1.359	1.348	1.358	1.350	1.354	0.004	0.006	0.0043	0.0038
C4-C5	1.446(2)	1.451	1.452	1.448	1.453	1.445	0.001	0.007	0.0048	0.0042
C4-C41	1.503(2)	1.505	1.499	1.500	1.501	1.493	0.002	0.010	0.0052	0.0064
C5-C10	1.402(2)	1.410	1.399	1.407	1.400	1.403	0.001	0.008	0.0045	0.0042
C5-C6	1.406(2)	1.410	1.404	1.408	1.405	1.405	0.001	0.004	0.0023	0.0020
C6-C7	1.376(2)	1.383	1.377	1.381	1.379	1.378	0.001	0.007	0.0042	0.0036
C7-C8	1.401(2)	1.406	1.401	1.405	1.403	1.402	0.001	0.005	0.0030	0.0024
C8-C9	1.391(2)	1.394	1.387	1.392	1.389	1.389	0.001	0.004	0.0026	0.0024
C9-C10	1.386(2)	1.395	1.390	1.393	1.392	1.390	0.004	0.009	0.0063	0.0058
Bond angles (°)	**Experimental**	**B3LYP**	**CAM-B3LYP**	**B3PW91**	**wB97XD**	**M06**	**Min dev.**	**Max dev.**	**RMS**	**MAE**
C2-O1-C10	121.3(1)	122.3	122.3	122.3	122.3	122.6	1.0	1.3	1.0668	1.06
O1-C10-C9	116.1(1)	116.3	116.2	116.2	116.1	116.4	0.1	0.3	0.1732	0.14
C5-C10-C9	122.9(1)	121.9	121.9	121.8	121.9	121.8	1.0	1.1	1.0412	1.04
O1-C2-O21	116.4(1)	117.5	117.8	117.5	117.7	117.6	1.1	1.4	1.2256	1.22
O1-C10-C5	121.0(1)	121.8	121.9	121.9	122.0	121.8	0.8	1.0	0.8832	0.88
O21-C2-C3	125.3(1)	126.6	126.1	126.5	126.0	126.6	0.7	1.3	1.0909	1.06
O1-C2-C3	118.3(1)	116.0	116.1	116.0	116.3	115.8	2.0	2.5	2.2658	2.26
C2-C3-C4	122.0(1)	123.2	123.0	123.2	123.0	123.2	1.0	1.2	1.1243	1.12
C3-C4-C41	121.2(1)	121.1	121.4	121.2	121.5	121.3	0.1	0.3	0.1732	0.16
C5-C4-C41	120.1(1)	120.2	119.9	120.2	119.9	120.0	0.1	0.2	0.1483	0.14
C3-C4-C5	118.7(1)	118.7	118.7	118.6	118.6	118.7	0.0	0.1	0.0632	0.20
C4-C5-C6	124.6(1)	124.7	124.6	124.7	124.6	124.6	0.0	0.1	0.0632	0.20
C4-C5-C10	118.6(1)	118.0	118.0	118.0	117.6	118.0	0.6	1.0	0.6986	0.68
C6-C5-C10	116.8(1)	117.3	117.4	117.3	117.4	117.4	0.5	0.6	0.5621	0.56
C5-C6-C7	121.5(1)	121.7	121.7	121.8	121.6	121.7	0.1	0.3	0.2098	0.20
C6-C7-C8	120.0(1)	119.5	119.5	119.5	119.5	119.5	0.0	0.5	0.5000	0.50
O81-C8-C9	122.6(1)	122.6	122.5	122.6	122.6	122.5	0.0	0.1	0.0632	0.04
C7-C8-C9	120.2(1)	120.4	120.4	120.3	120.4	120.5	0.1	0.3	0.2098	0.20
O81-C8-C7	117.2(1)	117.1	117.1	117.1	117.0	117.1	0.1	0.2	0.1265	0.12
C8-C9-C10	118.5(1)	119.2	119.1	119.2	119.1	119.1	0.6	0.7	0.6419	0.64

(a)　　　　(b)
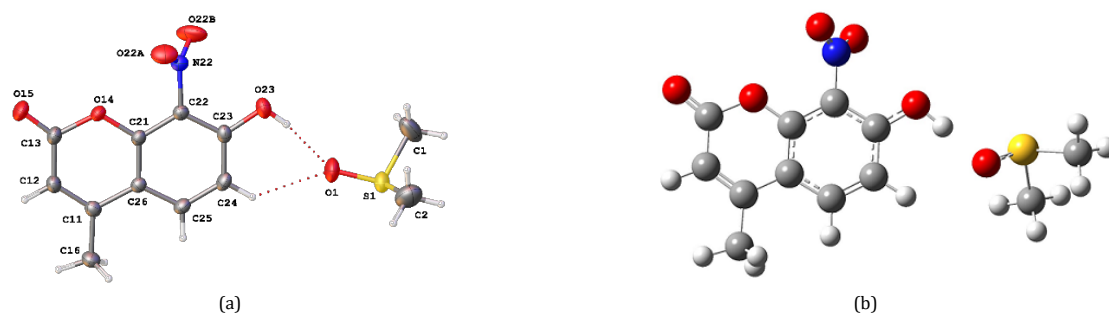
Figure 3. An ORTEP view and computationally optimized structure of 7-hydroxy-4-methyl-8-nitro-2*H*-chromen-2-one compound with (methylsulfinyl)methane (1:1, v:v).

Experimentally determined bond angles for O21-C2-C3, O1-C2-C3, C2-C3-C4, C3-C4-C41 and C5-C4-C41 which were 125.3(1), 118.3(1), 122.0(1), 121.2(1) and 120.1(1)° with the DFT calculated bond angles giving deviations between 0.1 and 2.5 °. Crystal data revealed that the bond angles of C3-C4-C5, C4-C5-C6, C4-C5-C10, C6-C5-C10 and C5-C6-C7 were experimentally determined as 118.7(1), 124.6(1), 18.6(1), 116.8(1) and 121.5(1)° with deviations between 0.001 and 1.0 ° representing the lowest and largest deviations, respectively, of the calculated values, from the experimental data. The bond angles of C4-C5-C10, C6-C5-C10, C5-C6-C7 and C6-C7-C8 were experimentally found to be 118.6(1), 116.8(1), 121.5(1) and 120.0(1)° while the computed values gave deviations between 0.1 and 1.0° from the experimental values. Crystal data revealed that the bond angles O81-C8-C9, C7-C8-C9, O81-C8-C7, and C8-C9-C10, which were 122.6(1), 120.2(1), 117.2(1) and 118.5(1)°, respectively, deviated from the calculated values by 0.1-0.7°.

Table 3 gives the results of the linear regression for theoretical and experimental bond lengths and bond angles for 7-hydroxy-4-methyl-2*H*-chromen-2-one (1). Linear regression analyzes were performed between the experimental and theoretical bond lengths and bond angles of 7-hydroxy-4-methyl-2*H*-chromen-2-one (1), using five density functionals (B3LYP, CAM-B3LYP, B3PW91, wB97XD, and M06) with the 6-311G(d,p) basis set. In these models, the experimental values were considered the dependent variable, whereas the theoretical values served as the independent variable. For the lengths of the bonds, all functionals exhibited strong linear correlations with the experimental data, with R^2 values ranging from 0.971 to 0.980. The CAM-B3LYP and wB97XD functionals yielded the highest coefficients of determination (R^2 = 0.980), indicating superior predictive performance. Slopes (b_1) were close to unity (0.912-0.937), suggesting a high degree of agreement. For the bond angles, the R^2 values ranged from 0.902 to 0.918, with wB97XD again showing the best coefficient of determination (R^2 = 0.918). The slopes for the bond angles (0.866-0.900) indicate a modest compression in the predicted values, and the relatively higher intercepts ($b_0 \approx$ 12-16°) reflect minor systematic deviations. In general, the regression results confirm that all five functionals provide statistically significant and reliable predictions of the experimental data.

Table 3. Linear regression for theoretical and experimental bond lengths (Å), and bond angles (°) for 7-hydroxy-4-methyl-2*H*-chromen-2-one (1) using B3LYP, CAM-B3LYP, B3PW91, wB97XD and M06 functionals and 6-311G(d,p) basis set.

DFT functional (Bond lengths)	b_0	b_1	*p*-value	R^2
B3LYP	0.095	0.928	< 0.00001	0.972
CAMB3LYP	0.112	0.920	< 0.00001	0.980
B3PW91	0.087	0.936	< 0.00001	0.973
wB97XD	0.122	0.912	< 0.00001	0.980
M06	0.089	0.937	< 0.00001	0.971
DFT functional (Bond angles)	b_0	b_1	*p*-value	R^2
B3LYP	15.142	0.873	< 0.00001	0.916
CAMB3LYP	11.894	0.900	< 0.00001	0.915
B3PW91	15.316	0.872	< 0.00001	0.915
wB97XD	12.526	0.895	< 0.00001	0.918
M06	16.019	0.866	< 0.00001	0.902

Table 4. Summary of theoretical and experimental bond lengths (Å), and bond angles (°) for 7-hydroxy-4-methyl-8-nitro-2*H*-chromen-2-one compound with (methylsulfinyl)methane (1:1) using B3LYP, CAM-B3LYP, B3PW91, wB97XD and M06 functionals and 6-311G(d,p) basis set (RMS: Root mean square, MAE: Mean absolute error).

Bond lengths (Å)	Experimental	B3LYP	CAM-B3LYP	B3PW91	wB97XD	M06	Min dev.	Max dev.	RMS	MAE
S1-C1	1.745(2)	1.824	1.804	1.812	1.807	1.807	0.059	0.079	0.066	0.066
S1-C2	1.639(2)	1.824	1.804	1.812	1.807	1.807	0.165	0.185	0.172	0.172
S1-O1	1.464(8)	1.535	1.526	1.529	1.519	1.519	0.055	0.071	0.062	0.062
S2-O2	1.455(1)	1.535	1.526	1.529	1.519	1.519	0.064	0.080	0.071	0.434
S2-C3	1.733(2)	1.824	1.804	1.811	1.807	1.807	0.071	0.091	0.078	0.078
S2-C4	1.640(2)	1.824	1.804	1.812	1.807	1.807	0.167	0.184	0.171	0.170
O14-C13	1.391(3)	1.406	1.390	1.399	1.349	1.389	0.100	0.042	0.020	0.014
O14-C21	1.364(3)	1.355	1.351	1.349	1.319	1.349	0.009	0.045	0.023	0.019
O22A-N22	1.233(4)	1.228	1.219	1.221	1.219	1.219	0.005	0.014	0.012	0.012
O22B-N22	1.181(4)	1.227	1.220	1.222	1.227	1.219	0.038	0.046	0.042	0.042
O23-C23	1.333(3)	1.333	1.327	1.328	1.464	1.327	0.005	0.131	0.059	0.030
N22-C22	1.455(3)	1.470	1.462	1.465	1.350	1.464	0.005	0.120	0.048	0.029
C11-C12	1.345(4)	1.358	1.348	1.357	1.501	1.350	0.001	0.143	0.070	0.038
C11-C16	1.492(4)	1.505	1.500	1.500	1.455	1.501	0.008	0.037	0.019	0.015
C12-C13	1.419(4)	1.452	1.453	1.449	1.393	1.455	0.030	0.026	0.032	0.032
C21-C22	1.386(3)	1.397	1.391	1.395	1.402	1.393	0.005	0.016	0.010	0.010
C21-C26	1.383(3)	1.411	1.400	1.408	1.396	1.402	0.013	0.028	0.021	0.020
C22-C23	1.392(3)	1.404	1.396	1.402	1.389	1.396	0.004	0.012	0.008	0.007
Bond angles (°)	**Experimental**	**B3LYP**	**CAM-B3LYP**	**B3PW91**	**wB97XD**	**M06**	**Min dev.**	**Max dev.**	**RMS**	**MAE**
O1-S1-C1	106.3(7)	105.6	105.4	105.6	105.6	105.6	0.7	0.9	0.744	0.740
O1-S1-C2	112.9(8)	105.8	105.6	105.9	105.5	105.5	7.0	7.4	7.242	7.240
C1-S1-C2	101.3(8)	97.8	98.0	97.8	97.6	97.6	3.3	3.7	3.543	3.540
C3-S2-C4	104.8(11)	97.8	98.0	97.8	97.6	97.6	6.8	7.2	7.042	7.040
O2-S2-C3	107.6(11)	105.6	105.4	105.9	005.6	105.6	1.7	2.2	1.986	1.980
O2-S2-C4	109.9(10)	105.8	105.6	105.6	105.5	105.5	4.1	4.4	4.301	4.300
C13-O14-C21	120.8(2)	122.2	122.2	122.2	122.1	122.1	1.3	1.4	1.361	1.360
O22B-N22-C22	119.3(3)	117.2	117.1	117.1	117.1	117.1	2.1	2.2	2.180	2.180
O22A-N22-O22B	123.7(2)	125.8	126.7	125.9	125.8	125.8	2.1	3.0	2.327	2.300
O22A-N22-C22	117.0(2)	117.0	117.3	116.9	117.0	117.0	0.1	0.3	0.141	0.080
C12-C11-C26	118.6(2)	118.9	118.8	118.8	121.4	118.7	0.1	0.3	1.266	0.720
C16-C11-C26	119.9(2)	120.1	119.9	120.1	119.8	119.8	0.1	0.2	0.141	0.120
C12-C11-C16	121.6(2)	121.0	121.3	121.1	118.7	121.4	0.1	2.3	1.353	0.900
C11-C12-C13	123.2(3)	123.2	122.9	123.1	122.9	122.9	0.1	0.3	0.237	0.200
O15 -C13-C12	127.5(2)	126.8	126.3	126.7	126.2	126.9	0.1	0.4	0.961	0.920
O14-C13-C12	117.2(2)	115.8	116.0	115.9	116.1	116.1	0.1	0.3	1.226	1.220
O14-C13-O15	115.3(2)	117.4	117.7	117.4	117.6	117.6	0.2	0.3	2.243	2.240
C22-C21-C26	121.0(2)	120.5	120.5	120.4	120.4	120.4	0.0	0.1	0.562	0.560
O14-C21-C26	122.3(2)	122.1	122.2	122.4	122.4	122.4	0.1	0.3	0.126	0.120
O14-C21-C22	116.6(2)	117.4	117.3	117.3	117.2	117.2	0.1	0.2	0.684	0.680
N22-C22-C21	119.3(2)	119.7	119.6	108.9	119.6	119.6	0.1	0.8	4.660	2.340
C21-C22-C23	121.3(2)	121.3	121.3	121.4	121.4	121.4	0.1	0.3	0.077	0.060
N22-C22-C23	119.5(2)	119.0	119.0	118.9	119.0	119.0	0.0	0.1	0.522	0.520
C22-C23-C24	117.6(2)	118.2	118.2	118.1	118.2	118.2	0.0	01	0.581	0.580
O23-C23-C24	123.8(2)	123.1	123.1	123.3	123.2	123.2	0.0	0.1	0.624	0.620
O23-C23-C22	118.6(2)	118.6	118.7	123.5	118.5	118.5	0.1	4.9	2.193	1.040
C23-C24-C25	120.7(2)	120.3	120.2	120.4	120.1	120.1	0.1	0.3	0.494	0.480

3.5. Comparison of the theoretical and experimental bond parameters for compound 2

Table 4 gives a summary of theoretical and experimental bond lengths and bond angles for compound **2** using B3LYP, CAM-B3LYP, B3PW91, wB97XD and M06 functionals and 6-311G(d,p) basis set. The bond lengths S1-C1, S1-C2, S1-O1, S2-O2, S2-C3 and S2-C4 for compound 2 were experimentally determined as 1.745(2), 1.639(2), 1.464(8), 1.455(1), 1.733(2) and 1.640(2) Å, respectively, while the calculated bond lengths gave deviations between 0.055 and 0.185 Å from the experimental values. The bond lengths of O14-C13, O14-C21, O22A-N22 and O22B-N22 were experimentally determined as 1.391(3), 1.364(3), 1.233(4) and 1.181(4) Å, respectively, while the computed values deviated by 0.009-0.100 Å from the experimental values. Crystallographically determined bond lengths of O23-C23, N22-C22, C11-C12 and C11-C16 were found at 1.333(3), 1.455(3), 1.345(4) and 1.492(4) Å while the computed values gave deviations between 0.005 and 0.143 Å. The bond lengths of C12-C13, C21-C22, C21-C26 and C22-C23 were experimentally determined as 1.419(4), 1.386(3), 1.383(3) and 1.392(3) Å with deviations between 0.004 and 0.030 Å representing the lowest and largest deviations, respectively, from the experimental values.

Table 5. Linear regression for theoretical and experimental bond lengths (Å), and bond angles (°) for 7-hydroxy-4-methyl-8-nitro-2*H*-chromen-2-one compound with (methylsulfinyl)methane (1:1) using B3LYP, CAM-B3LYP, B3PW91, wB97XD and M06 functionals and 6-311G(d,p) basis set.

DFT functional (Bond lengths)	b_0	b_1	*p*-value	R^2
B3LYP	0.314	0.758	< 0.00001	0.955
CAMB3LYP	0.293	0.777	< 0.00001	0.957
B3PW91	0.301	0.770	< 0.00001	0.956
wB97XD	0.363	0.730	< 0.00001	0.852
M06	0.298	0.774	< 0.00001	0.958
DFT functional (Bond angles)	b_0	b_1	*p*-value	R^2
B3LYP	26.398	0.781	< 0.00001	0.948
CAMB3LYP	26.849	0.777	< 0.00001	0.943
B3PW91	32.350	0.731	< 0.00001	0.877
wB97XD	27.603	0.771	< 0.00001	0.932
M06	27.284	0.773	< 0.00001	0.946
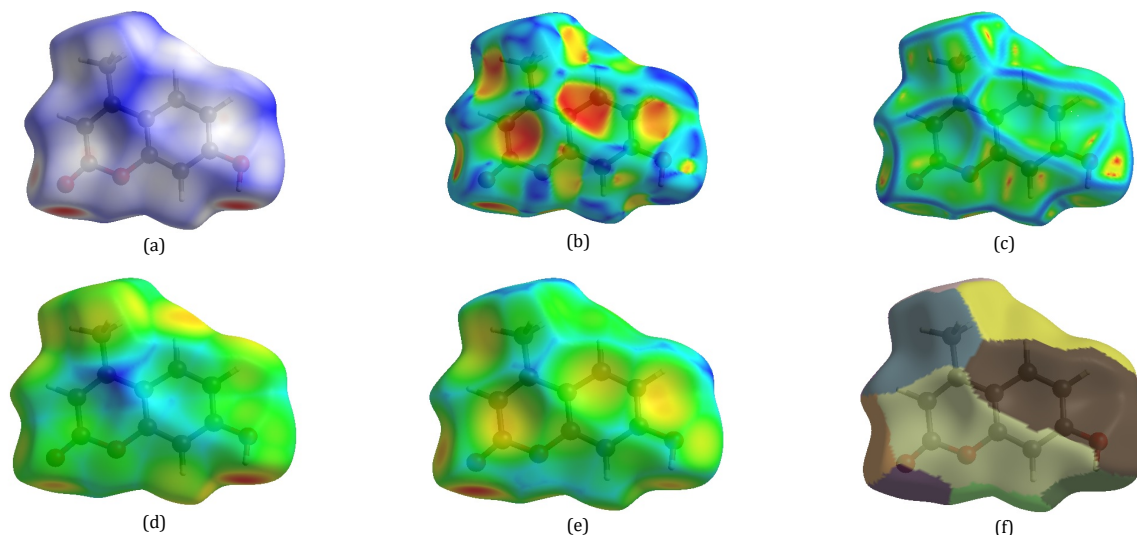
Figure 4. Hirshfeld surfaces mapped for (a) d_{norm} surfaces, (b) shape index, (c) curvedness, (d) d_i, (e) d_e, and (f) fragment patch of compound **1**.

The bond angles of O1-S1-C1, O1-S1-C2, C1-S1-C2, C3-S2-C4, O2-S2-C3 and O2-S2-C4 were experimentally found to be 106.3(7), 112.9(8), 101.3(8), 104.8(11), 107.6(11) and 109.9(10)°, while the computed values gave deviations of between 0.7 and 7.2° from the experimental values. Crystal data revealed that bond angles of C13-O14-C21, O22B-N22-C22, O22A-N22-O22B, O22A-N22-C22 and C12-C11-C26, were 120.8(2), 119.3(3), 123.7(2), 117.0(2) and 118.6(2), respectively, they deviated from the calculated values by 0.1-2.3°. The bond angles of C16-C11-C26, C12-C11-C16, C11-C12-C13, O15 -C13-C12 and O14-C13-C12 were experimentally determined as 119.9(2), 121.6(2), 123.2(3), 127.5(2) and 117.2(2) (1)°, while the computed values gave deviations of between 0.1 and 2.3° from the experimental values. Crystal structure data gave the experimentally determined bond angles for O14-C13-O15, C22-C21-C26, O14-C21-C26, O14-C21-C22 and N22-C22-C21 as 115.3(2), 121.0(2), 122.3(2), 116.6(2) and 119.3(2) respectively, which deviated from the computed values by 0.1 to 0.8°. The bond angles of N22-C22-C23, C22-C23-C24, O23-C23-C24, O23-C23-C22 and C23-C24-C25 were experimentally determined as 119.5(2), 117.6(2), 123.8(2), 118.6(2) and 120.7(2)°, while the computed values gave deviations of between 0.1 and 4.9° from the experimental data.

Linear regression analyses between experimental and theoretical bond lengths and bond angles of the 7-hydroxy-4-methyl-8-nitro-2*H*-chromen-2-one-(methylsulfinyl) methane (1:1) complex were performed using five DFT methods (B3LYP, CAM-B3LYP, B3PW91, wB97XD and M06) with the 6-311G(d,p) basis set. All models demonstrated statistically significant correlations (*p* < 0.00001). For the lengths of the bonds, the M06 functional showed the best predictive performance (R^2 = 0.958), closely followed by CAM-B3LYP and B3PW91. The slopes ranged from 0.730 to 0.777, with minor systematic deviations indicated by intercepts between 0.293 and 0.363. In

the case of bond angles, B3LYP and M06 yielded the highest R^2 values (0.948 and 0.946, respectively), with slopes between 0.731 and 0.781 and relatively higher intercepts (26.398-32.350°), suggesting consistent underprediction and slight systematic offsets. Overall, the M06 and CAM-B3LYP functionals offered the most reliable agreement with the experimental data for bond lengths, while B3LYP and M06 provided the best predictions for bond angles. Table 5 shows the results of the linear regression for the theoretical and experimental bond lengths (Å), and bond angles (°) for the 7-hydroxy-4-methyl-8-nitro-2H-chromen-2-one compound with (methylsulfinyl)methane (1:1) (2).

3.6. Hirshfeld surface analysis

A quantitative method for examining the interactions between molecules in a crystal structure is Hirshfeld surface analysis. Their crystal-packing behavior is described in depth. Crystal Explorer 3.1 software was used to map fingerprint plots and Hirshfeld surfaces [66]. The normalized contact distance (d_{norm}), which was calculated using the following equation and acquired with a high surface resolution and static color scale, served as a visual representation of the analysis.

According to Equation 1, rvdw is the atom's van der Waals radius, and de is the distance between the Hirshfeld surface and the closest nucleus outside the surface, and d_i is the corresponding distance between the nearest nucleus inside the surface [67]. The parameter d_{norm} is described by the surface with a red, white, and blue color scheme [68-70]. Inter-molecular interactions shorter than their vdW radii are indicated by bright red spots, whereas those longer than their vdW radii are indicated by blue spots. Their vdW radii add up to the white patches.
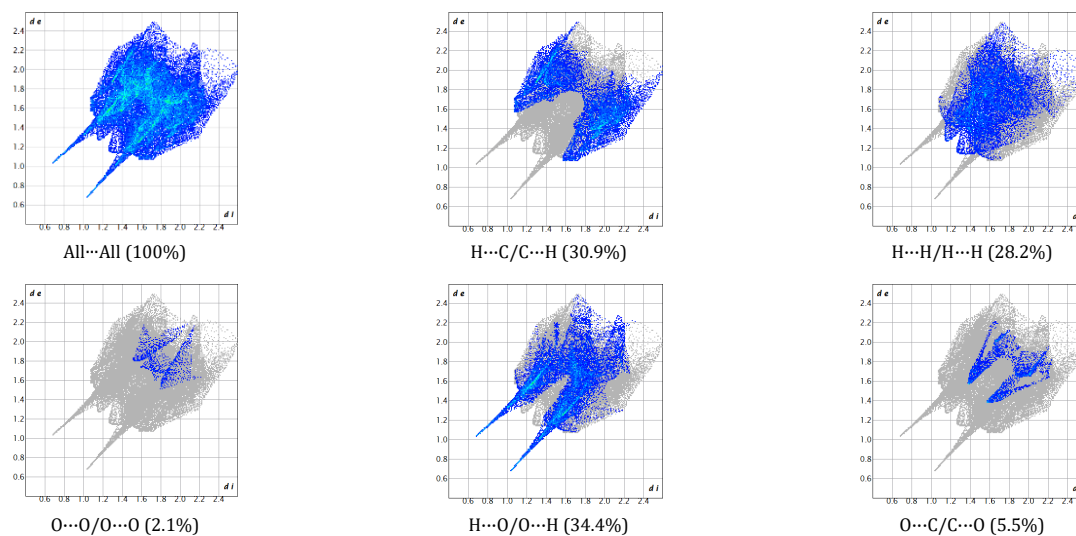
Figure 5. Relative contributions to the percentage of Hirshfeld surface area for the various intermolecular contacts for compound **1**.
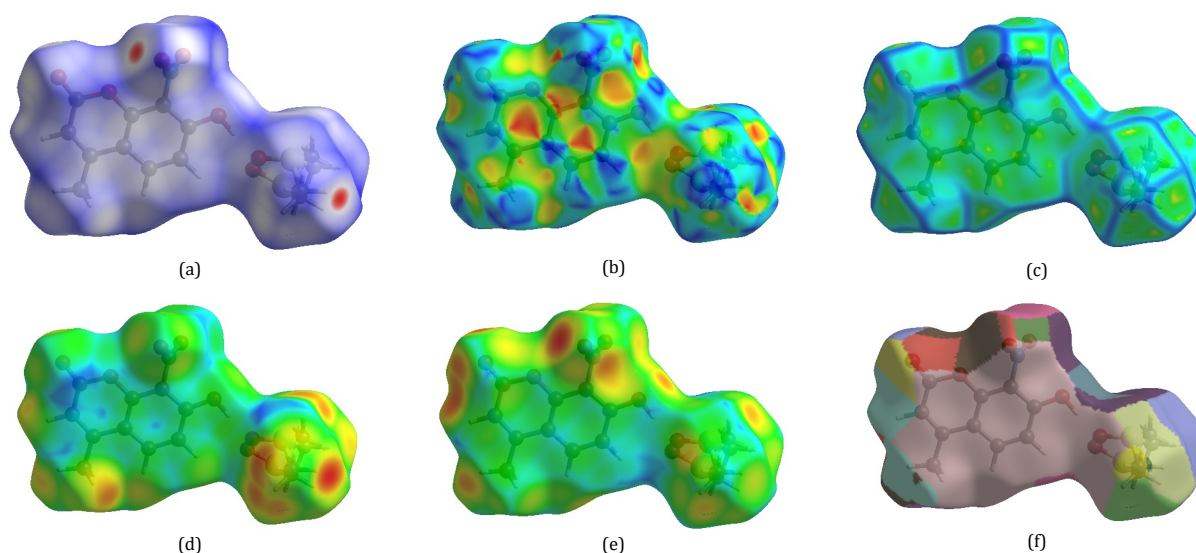

Figure 6. Hirshfeld surfaces mapped for (a) d_{norm} surfaces, (b) shape index, (c) curvedness, (d) d_i, (e) d_e and (f) fragment patch of compound **2**.

$$d_{norm} = \frac{d_i - r_i vdw}{r_i vdw} + \frac{d_e - r_e vdw}{r_e vdw} \tag{1}$$
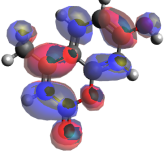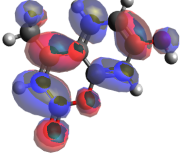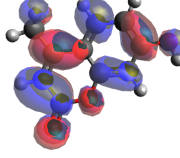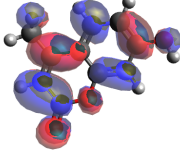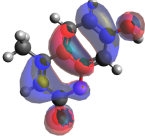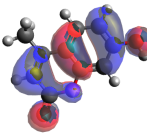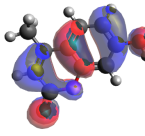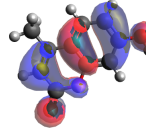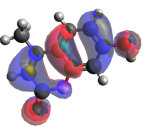
Figure 4 shows the molecular Hirshfield surfaces that were created using a standard (high) surface resolution. These surfaces include the d_{norm} surface, shape index, and curvedness of compound 1. Although d_i was mapped throughout the range of 0.6837 to 2.6269 Å, the d_{norm} surface was mapped on over the range of -0.6918 to 1.2749 Å. The shape index ranged from -1.0000 to 1.0000 Å, the fragment patch from 0.0000 to 13.0000 Å, the curvature from -4.0000 to 0.4000 Å, and the parameter de was between 0.6813 and 2.5157 Å.

The two-dimensional (2D) fingerprint plots from the Hirshfeld surface analyses of compound 1 are shown in Figure 5. They show the relative contribution (in percentage) of the major intermolecular contacts associated with it. Furthermore, the C-H (30.9%) and O-H (34.4%) fingerprint plots also provide information about the intermolecular hydrogen bonds and the contribution of the individual elements toward crystal packing. The 2D fingerprint plots complement the Hirshfeld surface by providing quantitative information on the nature and type of intermolecular contacts. The most significant interaction is H-H, which contributes 28.2% to the overall crystal packing. One

of the most important connections is the H-H interaction, which is represented by a single spike. Weak C-H···π interactions are the cause of the distinctive "*wings*" shown in the fingerprint plot of C-H contacts. On the form index, the blue triangles, which are represented by convex regions, show the ring atoms of the molecule inside the surface, while the red triangles, which are represented by concave regions, show π-stacking interactions. According to the 2D fingerprint plot, the C-H···π interactions, represented by the red triangles on the shape index mapping, have a contribution of 30.9%. The electron density of the surface curves around the chemical interactions, as indicated by the curvedness. Whereas strong curvature areas, which often tend to divide the surface into patches and indicate connections between nearby molecules, correlate with high values of curvedness, flat areas of the surface correspond to low levels of curvedness. π···π stacking interactions are indicated by a broad and flat area with a blue boundary. This molecule exhibits π···π stacking interactions to some extent.

Molecular Hirshfield surfaces comprising of d_{norm} surface, shape index, and curvedness of compound 1 were generated using a standard (high) surface resolution and are illustrated in Figure 6.

Table 6. HOMO-LUMO of compound **1** using B3LYP, CAM-B3LYP, B3PW91, wB97XD and M06 with the 6-311G(d,p) basis set.

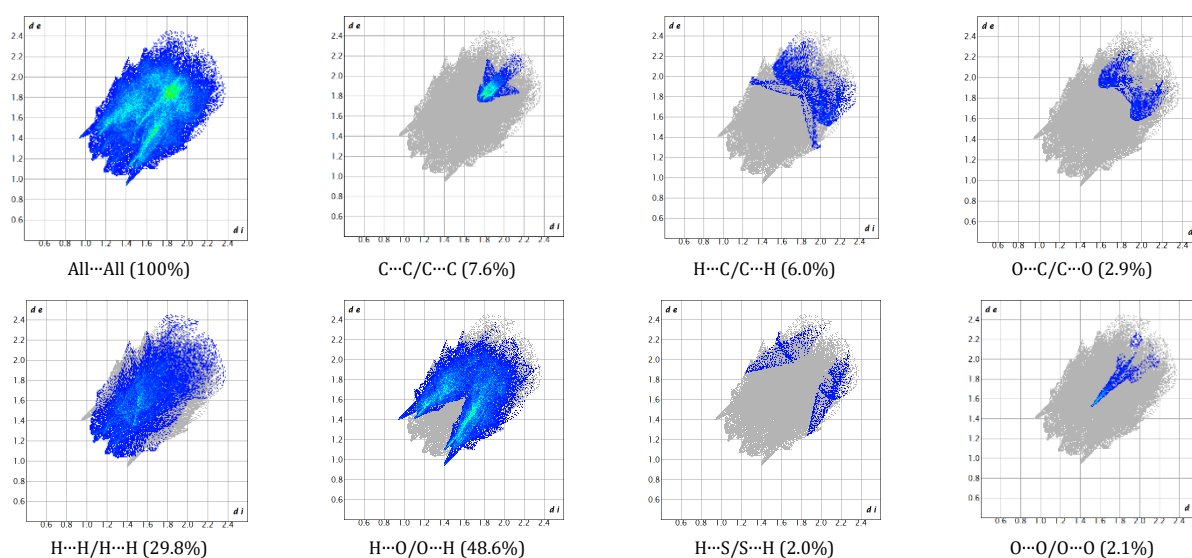|	B3LYP	CAM-B3LYP	B3PW91	Wb97XD	M06
LUMO					
HOMO					

Figure 7. Relative contributions to the percentage of Hirshfeld surface area for the various intermolecular contacts for compound **2**.

The d_{norm} surface was mapped on over the range of -0.2061 to 1.1877 Å, while d_i was mapped over the range of 0.9488 to 2.4042 Å. The parameter d_e was in the range of 0.9497 to 2.4758 Å, the shape index ranging from -1.0000 to 1.0000 Å, fragment patch 0.0000 to 32.0000 Å and curvature lying between -4.0000 to 0.4000 Å.

The two-dimensional (2D) fingerprint plots of compound 2 from Hirshfeld surface analysis are shown in Figure 7. It displays the proportional share (in percentage) of the main intermolecular interactions that are connected to it. By offering quantitative data on the kind and nature of intermolecular interactions, the 2D fingerprint plots enhance the Hirshfeld surface. O-H is the most significant interaction, accounting for 48.6% of the total crystal packing.

Furthermore, information regarding intermolecular hydrogen bonds and the different elements' contributions to the crystal packing may be found in the C-H (6.0%) and H-H (29.8%) fingerprint plots. Flat and sparse taperings in the fingerprint pattern of C-H contacts are compatible with very weak C-H⋯π interactions. On the form index, the blue triangles, which are represented by convex regions, show the ring atoms of the molecule inside the surface, while the red triangles, which are represented by concave regions, show π-stacking interactions. The electron density of the surface curves around the chemical interactions, as indicated by the curvedness. Whereas strong curvature areas, which often tend to divide the surface into patches and indicate connections between nearby molecules, correlate with high values of curvedness, flat areas of the surface correspond to low levels of curvedness. π⋯π stacking interactions are indicated by a broad and flat area with

a blue boundary. Curvedness indicates that there are no π⋯π stacking interactions in this molecule.
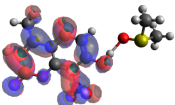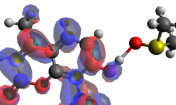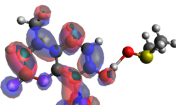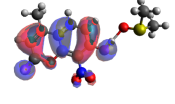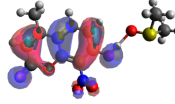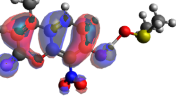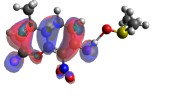
3.7. HOMO-LUMO analysis
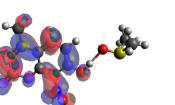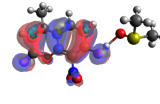
Table 6 shows the computed HOMO-LUMO energies for 7-hydroxy-4-methyl-2*H*-chromen-2-one (1). The frontier orbitals of compound 1 shows that the HOMO is delocalized over the entire molecule except the methyl group and some hydrogen atoms, while the LUMO is largely delocalized over the entire molecule except some hydrogen atoms. This indicates that during charge transfer in a reaction, the molecule is stabilized by delocalization of electrons over the entire molecule, which also confirms the susceptibility of some protons to substitution reaction. The delocalization of electrons in the HOMO and LUMO is consistent for all functionals and basis set except for a minor difference in orbital distribution.
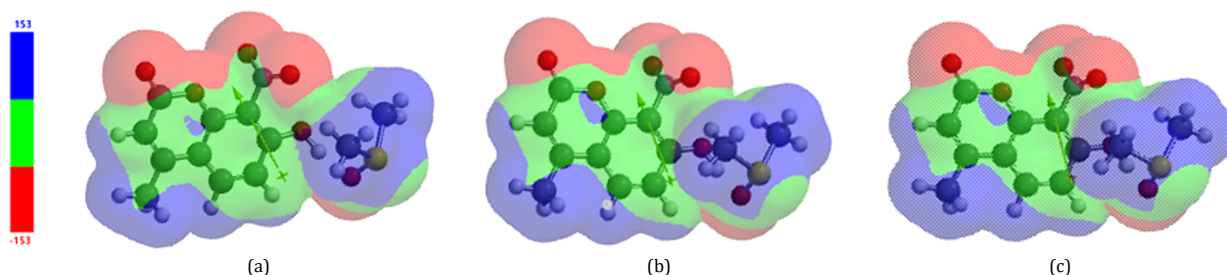
Table 7 gives the computed HOMO-LUMO energies for compound **2**. HOMO is delocalized over 7-hydroxy-4-methyl-8-nitro-2*H*-chromen-2-one with the exception of two protons on the methyl group and some protons on the coumarin ring with no contribution from methylsulfinyl)methane, while the LUMO is delocalized over the coumarin ring except the methyl group with partial contribution from the nitro group but no contribution from the dimethylsulfoxide group.

3.8. Molecular electrostatic potential maps

The electrostatic potential shows static charge distributions on a molecule.

Table 7. HOMO-LUMO of compound **2** using B3LYP, CAM-B3LYP, B3PW91, wB97XD and M06 with the 6-311G(d,p) basis set.

	B3LYP	CAM-B3LYP	B3PW91	wB97XD	M06
LUMO					
HOMO					

Figure 8. Molecular electrostatic potential maps (isosurface value = 0.02 au) of 7-hydroxy-4-methyl-8-nitro-2*H*-chromen-2-one compound with (methyl sulfinyl)methane (1:1) calculated at (A) B3LYP/6-311G(d,p), (B) M06/6-311G(d,p), (C) ωB97X-D/6-311G(d,p) level of theory. The red surface corresponds to a region of negative electrostatic potential, whereas the blue color corresponds to the positive potential. Positive and negative potentials in kJ/mol.

This property has been beneficial for analyzing and predicting molecular reactive behavior, indicating sites or regions of a molecule where an approaching electrophile/nucleophile is initially attracted. The MEP was calculated to predict reactive sites for electrophilic and nucleophilic attack for the 7-hydroxy-4-methyl-8-nitro-2*H*-chromen-2-one compound with (methyl sulfinyl) methane (1:1) studied. The positive regions (blue) are related to nucleophilic reactivity, and the negative regions (red) to electrophilic reactivity, shown in Figure 8.

4. Conclusions

7-Hydroxy-4-methyl-2*H*-chromen-2-one (compound 1) and 7-hydroxy-4-methyl-8-nitro-2*H*-chromen-2-one (compound 2) were synthesized and characterized using IR, NMR, GC-MS, and microanalysis. Compound 1 crystallized in the orthorhombic space group $P2_12_12_1$, while compound 2 crystallized in the monoclinic space group $P2_1/c$, according to the compound's single-crystal X-ray structure. The non-classical hydrogen bonding network holds the four molecules in each of the compounds' unit cells together. The computed and experimental data showed good internal consistency upon comparison. Linear regression analysis of the calculated and experimental parameters for compound 1 indicated that the functionals CAM-B3LYP and wB97XD produced the highest determination coefficients (R^2 = 0.980), indicating better predictive performance. For compound 2, the bond lengths were highly consistent with experimental data, while the regression analysis for the bond angles showed greater variability among the functionals. CAM-B3LYP gave the best agreement with the experiment (R^2 = 0.873, b_1 = 0.765), while wB97XD and M06 showed the weakest correlations.

Acknowledgements

Supporting information Ⓢ

CCDC-2419172 and 2419173 contain the supplementary crystallographic data for this paper. These data can be obtained free of charge via https://www.ccdc.cam.ac.uk/structures/, or by e-mailing data_request@ccdc.cam.ac.uk, or by contacting The Cambridge Crystallographic Data Centre, 12 Union Road, Cambridge CB2 1EZ, UK; fax: +44(0)1223-336033.

Disclosure statement ⒹⓈ

Conflict of interests: The authors declare that they have no conflict of interest.
Ethical approval: All ethical guidelines have been adhered.
Sample availability: Samples of the compounds are available from the author.

CRediT authorship contribution statement Ⓒⓡ

Conceptualization: Felix Odame; Methodology: Felix Odame; Software: Eric Hosten, Felix Odame; Validation: Eric Hosten, Felix Odame; Formal Analysis: Eric Hosten, Felix Odame, Albert Aniagyei, Nathaniel Owusu Boadi; Investigation: Felix Odame, Resources: Felix Odame; Data Curation: Felix Odame; Statistical analysis : Salifu Nanga; Writing - Original Draft: Felix Odame; Writing - Review and Editing: Felix Odame, Salifu Nanga, Nathaniel Owusu Boadi; Visualization: Felix Odame; Supervision: Felix Odame; Project Administration: Felix Odame.

ORCID ⒾⒹ and Email ✉

Felix Odame
✉ felixessah15@gmail.com
ⒾⒹ https://orcid.org/0000-0001-7651-8816
Nathaniel Owusu Boadi
✉ noboadi@gmail.com
ⒾⒹ https://orcid.org/0000-0003-2673-7011
Salifu Nanga
✉ snanga@uhas.edu.gh
ⒾⒹ https://orcid.org/0000-0002-3712-5013
Albert Aniagyei
✉ aaniagyei@uhas.edu.gh
ⒾⒹ https://orcid.org/0000-0002-9699-9300
Eric Hosten
✉ eric.hosten@mandela.ac.za
ⒾⒹ https://orcid.org/0000-0003-4173-2550

References

[1]. Lončarić, M.; Gašo-Sokač, D.; Jokić, S.; Molnar, M. Recent Advances in the Synthesis of Coumarin Derivatives from Different Starting Materials. *Biomolecules* **2020**, *10* (1), 151.

[2]. Bao, W.; Wang, Z.; Li, Y. Coumarin Synthesis via Knoevenagel Condensation in Moisture Stable Room Temperature Ionic Liquids. *J. Chem. Res.* **2003**, *2003* (5), 294–295.

[3]. Heravi, M. M.; Khaghaninejad, S.; Mostofi, M. Pechmann Reaction in the Synthesis of Coumarin Derivatives. *Adv. Heterocycl. Chem.* **2014**, 1–50.

[4]. Belavagi, N. S.; Deshpande, N.; Sunagar, M. G.; Khazi, I. A. A practical one-pot synthesis of coumarins in aqueous sodium bicarbonate via intramolecular Wittig reaction at room temperature. *RSC. Adv.* **2014**, *4* (75), 39667.

[5]. Olomola, T. O.; Klein, R.; Mautsa, N.; Sayed, Y.; Kaye, P. T. Synthesis and evaluation of coumarin derivatives as potential dual-action HIV-1 protease and reverse transcriptase inhibitors. *Bioorg. Med. Chem.* **2013**, *21* (7), 1964–1971.

[6]. Murray, R. D. H.; Ballantyne, M. M. Claisen Rearrangements—I. *Tetrahedron* **1970**, *26* (19), 4667–4671.

[7]. Vekariya, R. H.; Patel, H. D. Recent Advances in the Synthesis of Coumarin Derivatives via Knoevenagel Condensation: A Review. *Synth. Commun.* **2014**, *44* (19), 2756–2788.

[8]. He, X.; Yan, Z.; Hu, X.; Zuo, Y.; Jiang, C.; Jin, L.; Shang, Y. FeCl₃-Catalyzed Cascade Reaction: An Efficient Approach to Functionalized Coumarin Derivatives. *Synth. Commun.* **2014**, *44* (10), 1507–1514.

[9]. Prahadeesh, N.; Sithambaresan, M.; Mathiventhan, U. A Study on Hydrogen Peroxide Scavenging Activity and Ferric Reducing Ability of Simple Coumarins. *Emerg. Sci. J.* **2018**, *2* (6), 417–427.

[10]. Patil, S. B.; P., G.; Jalde, S. S. medicinal significance of novel coumarins: A review. *Int. J. Curr. Pharm. Sci.* **2021**, 1–5.

[11]. Naseri, M.; Monsef-Esfahani, H.; Saeidnia, S.; Dastan, D.; Gohari, A. Antioxidative Coumarins from the Roots of Ferulago subvelutina. *Asian. J. Chem.* **2013**, *25* (4), 1875–1878.

[12]. Kumar, S.; Arora, A.; Kumar, R.; Senapati, N. N.; Singh, B. K. Recent advances in synthesis of sugar and nucleoside coumarin conjugates and their biological impact. *Carbohydr. Res.* **2023**, *530*, 108857.

[13]. Barot, K. P.; Jain, S. V.; Kremer, L.; Singh, S.; Ghate, M. D. Recent advances and therapeutic journey of coumarins: current status and perspectives. *Med. Chem. Res.* **2015**, *24* (7), 2771–2798.

[14]. Cheke, R. S.; Patel, H. M.; Patil, V. M.; Ansari, I. A.; Ambhore, J. P.; Shinde, S. D.; Kadri, A.; Snoussi, M.; Adnan, M.; Kharkar, P. S.; Pasupuleti, V. R.; Deshmukh, P. K. Molecular insights into coumarin analogues as antimicrobial agents: Recent developments in drug discovery. *Antibiotics (Basel)* **2022**, *11*, 566.

[15]. Abdou, M. M. 3-Acetyl-4-hydroxycoumarin: Synthesis, reactions and applications. *Arab. J. Chem.* **2017**, *10*, S3664–S3675.

[16]. Al-Ayed, A. S. Synthesis, Spectroscopy and Electrochemistry of New 3-(5-Aryl-4,5-Dihydro-1H-Pyrazol-3-yl)-4-Hydroxy-2H-Chromene-2-One 4, as a Novel Class of Potential Antibacterial and Antioxidant Derivatives. *Int. J. Org. Chem.* **2011**, *01* (03), 87–96.

[17]. Al-Majedy, Y. K.; Kadhum, A. A.; Al-Amiery, A. A.; Mohamad, A. B. Coumarins: The Antimicrobial agents. *Syst. Rev. Pharm. SRP.* **2017**, *8* (1), 62–70.

[18]. Jumal, J.; Norhanis Sakinah, Synthesis, Characterization, and Applications of Coumarin Derivatives: A Short Review. *MJoSHT.* **2021**, *7* (1), 62–68.

[19]. Liu, H.; Ren, Z.; Wang, W.; Gong, J.; Chu, M.; Ma, Q.; Wang, J.; Lv, X. Novel coumarin-pyrazole carboxamide derivatives as potential topoisomerase II inhibitors: Design, synthesis and antibacterial activity. *Eur. J. Med. Chem.* **2018**, *157*, 81–87.

[20]. Sahoo, J.; Kumar Mekap, S.; Sudhir Kumar, P. Synthesis, spectral characterization of some new 3-heteroaryl azo 4-hydroxy coumarin derivatives and their antimicrobial evaluation. *J. Taibah. Univ. Sci.* **2015**, *9* (2), 187–195.

[21]. Vekariya, R. H.; Patel, K. D.; Rajani, D. P.; Rajani, S. D.; Patel, H. D. A one pot, three component synthesis of coumarin hybrid thiosemicarbazone derivatives and their antimicrobial evolution. *J. Assoc. Arab. Univ. Basic Appl. Sci.* **2017**, *23* (1), 10-19.

[22]. Basanagouda, M.; Shivashankar, K.; Kulkarni, M. V.; Rasal, V. P.; Patel, H.; Mutha, S. S.; Mohite, A. A. Synthesis and antimicrobial studies on novel sulfonamides containing 4-azidomethyl coumarin. *Eur. J. Med. Chem.* **2010**, *45* (3), 1151–1157.

[23]. Villa-Martínez, C. A.; Magaña-Vergara, N. E.; Rodríguez, M.; Mojica-Sánchez, J. P.; Ramos-Organillo, A. A.; Barroso-Flores, J.; Padilla-Martínez, I. I.; Martínez-Martínez, F. J. Synthesis, Optical Characterization in Solution and Solid-State, and DFT Calculations of 3-Acetyl and 3-(1′-(2′-Phenylhydrazono)ethyl)-coumarin-(7)-substituted Derivatives. *Molecules* **2022**, *27* (12), 3677.

[24]. Vyas, K.; Nimavat, K.; Jani, G.; Hathi, M. V. Synthesis and Antimicrobial Activity of Coumarin Derivatives Metal Complexes: An in Vitro Evaluation. *Orbital: Electron. J. Chem.* **2009**, *1* (2), 183–192.

[25]. Wei, Y.; Li, S.; Hao, S. New angular oxazole-fused coumarin derivatives: synthesis and biological activities. *Nat. Prod. Res.* **2017**, *32* (15), 1824–1831.

[26]. Chen, L. Z.; Sun, W. W.; Bo, L.; Wang, J. Q.; Xiu, C.; Tang, W. J.; Shi, J. B.; Zhou, H. P.; Liu, X. H. New arylpyrazoline-coumarins: Synthesis and anti-inflammatory activity. *Eur. J. Med. Chem.* **2017**, *138*, 170–181.

[27]. Pu, W.; Lin, Y.; Zhang, J.; Wang, F.; Wang, C.; Zhang, G. 3-Arylcoumarins: Synthesis and potent anti-inflammatory activity. *Bioorg. Med. Chem. Lett* 2014, *24* (23), 5432–5434.

[28]. Olmedo, D.; Sancho, R.; Bedoya, L. M.; López-Pérez, J. L.; Del Olmo, E.; Muñoz, E.; Alcamí, J.; Gupta, M. P.; San Feliciano, A. 3-Phenylcoumarins as Inhibitors of HIV-1 Replication. *Molecules* **2012**, *17* (8), 9245–9257.

[29]. Salem, M.; Marzouk, M.; El-Kazak, A. Synthesis and Characterization of Some New Coumarins with in Vitro Antitumor and Antioxidant Activity and High Protective Effects against DNA Damage. *Molecules* **2016**, *21* (2), 249.

[30]. Emami, S.; Dadashpour, S. Current developments of coumarin-based anti-cancer agents in medicinal chemistry. *Eur. J. Med. Chem.* **2015**, *102*, 611–630.

[31]. Keri, R. S.; B.S., S.; Nagaraja, B. M.; Santos, M. A. Recent progress in the drug development of coumarin derivatives as potent antituberculosis agents. *Eur. J. Med. Chem.* **2015**, *100*, 257–269.

[32]. Akoudad, S.; Darweesh, S. K.; Leening, M. J.; Koudstaal, P. J.; Hofman, A.; van der Lugt, A.; Stricker, B. H.; Ikram, M. A.; Vernooij, M. W. Use of Coumarin Anticoagulants and Cerebral Microbleeds in the General Population. *Stroke* **2014**, *45* (11), 3436–3439.

[33]. Hassan, M. Z.; Osman, H.; Ali, M. A.; Ahsan, M. J. Therapeutic potential of coumarins as antiviral agents. *Eur. J. Med. Chem* **2016**, *123*, 236–255.

[34]. Wijayabandara, M. D.; Choudhary, M. I.; Wijayabandara, M. D.; Adhikari, A. Scopoletin – an anti-hyperglycemic Coumarin from the fruit of Averrhoa carambola L. (Star fruit). *Pharm. J. SL.* **2017**, *7*, 51.

[35]. Al-Amiery, A. A.; Al-Majedy, Y. K.; Kadhum, A. A.; Mohamad, A. B. Novel macromolecules derived from coumarin: synthesis and antioxidant activity *Sci. Rep.* **2015**, *5* (1), 11825.

[36]. Matos, M.; Mura, F.; Vazquez-Rodriguez, S.; Borges, F.; Santana, L.; Uriarte, E.; Olea-Azar, C. Study of Coumarin-Resveratrol Hybrids as Potent Antioxidant Compounds. *Molecules* **2015**, *20* (2), 3290–3308.

[37]. Pérez-Cruz, K.; Moncada-Basualto, M.; Morales-Valenzuela, J.; Barriga-González, G.; Navarrete-Encina, P.; Núñez-Vergara, L.; Squella, J.; Olea-Azar, C. Synthesis and antioxidant study of new polyphenolic hybrid-coumarins. *Arab. J. Chem.* **2018**, *11* (4), 525–537.

[38]. Nagamallu, R.; Srinivasan, B.; Ningappa, M. B.; Kariyappa, A. K. Synthesis of novel coumarin appended bis(formylpyrazole) derivatives: Studies on their antimicrobial and antioxidant activities. *Bioorg. Med. Chem Lett.* **2016**, *26* (2), 690–694.

[39]. Anand, P.; Singh, B.; Singh, N. A review on coumarins as acetylcholinesterase inhibitors for Alzheimer's disease. *Bioorg. Med. Chem.* **2012**, *20* (3), 1175–1180.

[40]. Bagheri, S. M.; Khoobi, M.; Nadri, H.; Moradi, A.; Emami, S.; Jalili-Baleh, L.; Jafarpour, F.; Homayouni Moghadam, F.; Foroumadi, A.; Shafiee, A. Synthesis and Anticholinergic Activity of 4-hydroxycoumarin Derivatives Containing Substituted Benzyl-1,2,3-triazole Moiety. *Chem. Biol. Drug. Des.* **2015**, *86* (5), 1215–1220.

[41]. Razavi, S. F.; Khoobi, M.; Nadri, H.; Sakhteman, A.; Moradi, A.; Emami, S.; Foroumadi, A.; Shafiee, A. Synthesis and evaluation of 4-substituted coumarins as novel acetylcholinesterase inhibitors. *Eur. J. Med. Chem.* **2013**, *64*, 252–259.

[42]. Odame, F.; Tshentu, Z. R.; Lobb, K. Solvent promoted tautomerism in thione-containing tetraazatricyclics: evidence from 1H NMR spectroscopy and transition state studies. *J. Mol. Model* **2022**, *28*, 215.

[43]. Gastaca, B.; Sánchez, H. R.; Menestrina, F.; Caputo, M.; Schiavoni, M. d.; Furlong, J. J. Thiosemicarbazones Synthesized from Acetophenones: Tautomerism, Spectrometric Data, Reactivity and Theoretical Calculations. *IJAMSC.* **2019**, *07* (02), 19–34.

[44]. Bečić, E.; Dedić, M.; Imamović, B.; Špirtović-Halilović, S.; Omeragić, E. Substituent and Solvent Effects on the Spectral Properties of 3 Substituted Derivatives of 4-Hydroxycoumarin. *Kem. U. Ind.* **2024**, *73* (1–2), 1–6.

[45]. Bruker (2009). APEX2. Bruker AXS Inc., Madison, Wisconsin, USA.

[46]. Sheldrick, G. M. A short history of *SHELX. Acta. Crystallogr. A. Found. Crystallogr.* **2007**, *64* (1), 112–122.

[47]. Hübschle, C. B.; Sheldrick, G. M.; Dittrich, B. *ShelXle*: a Qt graphical user interface for*SHELXL. J. Appl. Crystallogr.* **2011**, *44* (6), 1281–1284.

[48]. Farrugia, L. J. *ORTEP*-3 for Windows - a version of*ORTEP*-III with a Graphical User Interface (GUI). *J. Appl. Crystallogr.* **1997**, *30* (5), 565–565.

[49]. Macrae, C. F.; Bruno, I. J.; Chisholm, J. A.; Edgington, P. R.; McCabe, P.; Pidcock, E.; Rodriguez-Monge, L.; Taylor, R.; van de Streek, J.; Wood, P. A. *Mercury CSD 2.0*– new features for the visualization and investigation of crystal structures. *J. Appl. Crystallogr.* **2008**, *41* (2), 466–470.

[50]. Spek, A. L. Structure Validation in Chemical Crystallography. *Acta Crystallogr. D Biol. Crystallogr.* **2009**, *65* (Pt 2), 148–155.

[51]. Rodríguez, S. E.; Hernandez-Fernández, E.; Vázquez, M. A.; García-Revilla, M. A.; Lagunas-Rivera, S. DFT Computational Analysis of Photophysical (Linear and Non-linear) and Photochemical Parameters for the Design of New Coumarins as Photocatalyst. *Top. Catal.* **2023**, *67* (5-8), 520–529.

[52]. Gawad, S. A.; Sakr, M. A. Spectroscopic investigation, DFT and TD-DFT calculations of 7-(Diethylamino) Coumarin (C466). *J. Mol. Struc.* **2022**, *1248*, 131413.

[53]. Hagar, M.; Ahmed, H. A.; Alhaddadd, O. A. DFT Calculations and Mesophase Study of Coumarin Esters and Its Azoesters. *Crystals (Basel)* **2018**, *8* (9), 359.

[54]. Frisch, M. J.; Trucks, G. W.; Schlegel, H. B.; Scuseria, G. E.; Robb, M. A.; Cheeseman, J. R.; Montgomery, J. A.; Vreven, T.; Kudin, K. N.; Burant, J. C.; Millam, J. M.; Iyengar, S. S.; Tomasi, J.; Barone, V.; Mennucci, B.; Cossi, M.; Scalmani, G.; Rega, N.; Petersson, G. A.; Nakatsuji, H.; Hada, M.; Ehara, M.; Toyota, K.; Fukuda, R.; Hasegawa, J.; Ishida, M.; Nakajima, T.; Honda, Y.; Kitao, O.; Nakai, H.; Klene, M.; Li, X.; Knox, J. E.; Hratchian, H. P.; Cross, J. B.; Adamo, C.; Jaramillo, J.; Gomperts, R.; Stratmann, R. E.; Yazyev, O.; Austin, A. J.; Cammi, R.; Pomelli, C.; Ochterski, J. W.; Ayala, P. Y.; Morokuma, K.; Voth, G. A.; Salvador, P.; Dannenberg, J. J.; Zakrzewski, V. G.; Dapprich, S.; Daniels, A. D.; Strain, M. C.; Farkas, O.; Malick, D. K.; Rabuck, A. D.; Raghavachari, K; Foresman, J. B.; Ortiz, J. V.; Cui, Q.; Baboul, A. G.; Clifford, S.; Cioslowski, J.; Stefanov, B. B.; Liu, G.; Liashenko, A.; Piskorz, P.; Komaromi, I.; Martin, R. L.; Fox, D. J.; Keith, T.; Al-Laham, M. A.; Peng, C. Y.; Nanayakkara, A.; Challacombe, M.; Gill, P. M. W.; Johnson, B.; Chen, W.; Wong, M. W.; Gonzalez, C.; Pople, J. A. Gaussian, Inc., Wallingford CT, 2004.

[55]. Padmaja, L.; Ravikumar, C.; Sajan, D.; Hubert Joe, I.; Jayakumar, V. S.; Pettit, G. R.; Faurskov Nielsen, O. Density functional study on the structural conformations and intramolecular charge transfer from the vibrational spectra of the anticancer drug combretastatin-A2. *J. Raman Spectroscopy* **2008**, *40* (4), 419–428.

[56]. Poiyamozhi, A.; Sundaraganesan, N.; Karabacak, M.; Tanrıverdi, O.; Kurt, M. The spectroscopic (FTIR, FT-Raman, UV and NMR), first-order hyperpolarizability and HOMO–LUMO analysis of 4-amino-5-chloro-2-methoxybenzoic acid. *J. Mol. Struc.* **2012**, *1024*, 1–12.

[57]. Suresh, C. H.; Remya, G. S.; Anjalikrishna, P. K. Molecular electrostatic potential analysis: A powerful tool to interpret and predict chemical reactivity. *WIREs Comput. Mol. Sci.* **2022**, *12* (5), e1601 https://doi.org/10.1002/wcms.1601.

[58]. Nakamura, S.; Kobayashi, T.; Takata, A.; Uchida, K.; Asano, Y.; Murakami, A.; Goldberg, A.; Guillaumont, D.; Yokojima, S.; Kobatake, S.; Irie, M. Quantum yields and potential energy surfaces: a theoretical study. *J. Phys. Org. Chem.* **2007**, *20* (11), 821–829.

[59]. Gadre, S. R.; Suresh, C. H.; Mohan, N. Electrostatic Potential Topology for Probing Molecular Structure, Bonding and Reactivity. *Molecules* **2021**, *26* (11), 3289.

[60]. Odame, F.; Hosten, E. C.; Betz, R.; Krause, J.; Frost, C. L.; Lobb, K.; Tshentu, Z. R. Synthesis, characterization, computational studies and DPPH scavenging activity of some triazatetracyclic derivatives. *J. Iran. Chem. Soc.* **2021**, *18* (8), 1979–1995.

[61]. Odame, F.; Kleyi, P.; Hosten, E.; Betz, R.; Lobb, K.; Tshentu, Z. The Formation of 2,2,4-Trimethyl-2,3-dihydro-1H-1,5-Benzodiazepine from 1,2-Diaminobenzene in the Presence of Acetone. *Molecules* **2013**, *18* (11), 14293–14305.

[62]. Odame, F.; Schoeman, R.; Krause, J.; Hosten, E. C.; Tshentu, Z. R.; Frost, C. Synthesis, characterization, crystal structures, and anticancer activity of some new 2,3-dihydro-1,5-benzoxazepines. *Med. Chem. Res.* **2021**, *30* (4), 987–1004.

[63]. Odame, F.; Hosten, E. C.; Lobb, K.; Tshentu, Z. Ultrasound promoted synthesis, characterization and computational studies of some thiourea derivatives. *J. Mol. Struc.* **2020**, *1216*, 128302.

[64]. Odame, F. Benzoyl isothiocyanates derived ligands as potential HIV-1 protease inhibitors and their reactions with gold ions, PhD Thesis, Nelson Mandela University, Faculty of Science, Department of Chemistry, 2016 https://core.ac.uk/download/pdf/224300821.pdf

[65]. Odame, F.; Hosten, E.; Betz, R.; Lobb, K.; Tshentu, Z. Characterization and Computational Studies of 2-(Benzamido)Thiazol-5-yl Benzoate. *J. Struct. Chem.* **2019**, *60* (1), 136–142.

[66]. Spackman, P. R.; Turner, M. J.; McKinnon, J. J.; Wolff, S. K.; Grimwood, D. J.; Jayatilaka, D.; Spackman, M. A. *CrystalExplorer*: a program for Hirshfeld surface analysis, visualization and quantitative analysis of molecular crystals. *J. Appl. Crystallogr.* **2021**, *54* (3), 1006–1011.

[67]. Al-Wahaibi, L. H.; Joubert, J.; Blacque, O.; Al-Shaalan, N. H.; El-Emam, A. A. Crystal structure, Hirshfeld surface analysis and DFT studies of 5-(adamantan-1-yl)-3-[(4-chlorobenzyl)sulfanyl]-4-methyl-4H-1,2,4-triazole, a potential 11β-HSD1 inhibitor. *Sci. Rep.* **2019**, *9* (1), https://doi.org/10.1038/s41598-019-56331-z.

[68]. Spackman, M. A.; Jayatilaka, D. Hirshfeld surface analysis. *CrystEngComm.* **2009**, *11* (1), 19–32.

[69]. Odame, F.; Madanhire, T.; Hosten, E. C. Crystal Structure and Hirshfeld Surface Analysis of 3-(pyrrolidine-1-carbonyl)-2H-Chromen-2-One. *J. Struct. Chem.* **2024**, *65* (7), 1305–1316.

[70]. Odame, F.; Madanhire, T.; Hosten, E. C.; Lobb, K. Crystal Structure, Hirshfeld Surface Analysis and Computational Studies of Two Benzo[b][1,4]Diazepine Derivatives. *J. Struct. Chem.* **2023**, *64* (12), 2326–2342.